PHYSICAL REVIEW E VOLUME 49, NUMBER 5 MAY 1994

Simulations of rf glow discharges in SF_6 by the relaxation continuum model: Physical structure and function of the narrow-gap reactive-ion etcher

Nobuhiko Nakano, Naohiko Shimura, Zoran Lj. Petrović,* and Toshiaki Makabe
Department of Electrical Engineering, Faculty of Science and Technology, Keio University, 3-14-1 Hiyoshi, Yokohama 223, Japan
(Received 1 July 1993)

A capacitively-coupled reactive ion etcher (RIE) can operate, even under high pressure conditions, for dry etching. Most of the etching gases are known to be strongly electronegative. The spatiotemporal structure of an ideal narrow-gap RIE with parallel plate geometry in an SF_6 discharge is investigated over the pressure range of 0.05–0.5 Torr at 13.56 MHz, using numerical simulations based on the relaxation continuum model. The rf plasma consists of a majority of positive and negative ions and a minority of more mobile electrons. The functionality of the narrow-gap RIE under typical operating conditions is due to the appearance of a double layer in front of the instantaneous anode. The double layer serves as the source of beamlike ions and virgin radicals immediately in front of the electrode surface. A narrower sheath width is realized compared with that found in electropositive gases. The maintenance of the rf discharge is accomplished by ionization at the double layer, while detached electrons from the negative ions have no significant influence on the function or the structure of the SF_6 discharge.

PACS number(s): 52.65.+z, 52.80.Pi, 52.25.Fi, 52.25.Jm

I. INTRODUCTION

Dry etching in a nonequilibrium-reactive plasma is one of many established techniques in the fabrication on microelectronic devices. Most of the source gases used in dry etching are electronegative gases which produce negative ions by electron impact on neutral molecules. The reactive species are produced by a capacitively or inductively coupled radio frequency (rf) discharge, a microwave discharge, or an electron cyclotron resonance plasma. Surprisingly, the capacitively coupled reactive ion etcher (RIE) with parallel plate geometry operates even under relatively high pressure conditions, up to several Torr, as a submicrometer pattern etcher [1]. Dry etching of silicon and polycrystalline tungsten film has been performed by an RIE in a SF_6 rf discharge [2,3]. Although several capacitive rf plasma simulations have been performed for electronegative gases [4–8], the functional properties of the discharge in the RIE have only been briefly discussed.

In a preceding paper (hereafter referred to as R1 [9]), experimental results from space-time resolved optical emission spectroscopy on SF_6 rf discharges have been discussed for a range of pressures between 0.05 Torr and 1.0 Torr and for frequencies of 100 kHz, 800 kHz, and 13.56 MHz. A range of powers was also studied, from the minimum sustaining power to as high as 100 W (2 $\mathrm{W\,cm^{-2}}$). In order to obtain information on the electron kinetics, 10% nitrogen was added to the SF_6. The first negative band of nitrogen from $N_2^+(B\,^2\Sigma_u^+)$ was used to study the high-energy electrons, while the second positive band from $N_2(C\,^3\Pi_u)$ gave information on the behavior of the middle-energy electrons. The systematic and absolute measurements yielded several distinct features of the kinetics in SF_6 rf discharges.

Among these features is the double layer formed in front of the instantaneous anode. The double layer induced emission is normally the most prominent feature in the emission profiles, at both low and high frequencies. The net excitation rate profile for 13.56 MHz and higher power, 1040 $\mathrm{mW\,cm^{-2}}$, shows a significant peak close to the instantaneous anode. This is consistent with the appearance of the sharp current peak delayed in comparison to the applied voltage, i.e., "inductive behavior." This is due to the electron density increase where the field becomes stronger at the time when the double layer is formed. This can be confirmed by comparing the wave forms produced by $N_2^+(B\,^2\Sigma_u^+)$ and $N_2(C\,^3\Pi_u)$ emission; the electrons in the double layer have a higher energy than those in the bulk plasma.

Emission peaks close to the cathode are also normally observable, corresponding to excitation by reflected, wave riding, stochastic heated electrons at 13.56 MHz [10–14] and γ electrons at 100 and 800 kHz. It should be stressed that there is no evidence of a contribution due to γ electrons at 13.56 MHz under low- or high-power conditions in the space-time-resolved excitation profiles. The relative importance of the peaks near the cathode increases as the power increases, and a peak appears in the current wave form at the time of the cathode emission peak. This feature is usually in phase, or even lagging behind the voltage wave form, resulting in inductive voltage-current characteristics.

The emission from the bulk plasma, at both low and high frequencies, is due to lower-energy electrons in the

*Present address: Institute of Physics, University of Belgrade, P.O. Box 86, 11080 Zemun, Yugoslavia.

 ©1994 The American Physical Society

relatively high bulk field. At 800 kHz and 0.1 Torr for the lowest powers, it is found that the bulk electrons are transported to the opposite electrode, as the polarity of the voltage begins to change.

A strongly electronegative gas, such as SF_6, will lead to a higher abundance of negative ions and the phenomena described above. These phenomena have been predicted by calculations and postulated on the basis of experimental results. The modulation of the negative charge density leads to the double layer formation, but the layer may also occur due to the strongly localized detachment of electrons from the negative ions. The detailed mechanism for the initial stage of the double layer formation and its further development could not be clarified in paper R1, since numerical modeling results, which include detailed kinetics of electrons and ions in the rf discharge, were required.

In a following paper (referred to as R2 [15]), external electrical characteristics of the parallel plate rf discharge in SF_6 were measured for pressures of 0.05, 0.1, and 1.0 Torr between frequencies of 20 kHz and 20 MHz. In particular, the minimum sustaining voltage of a glow plasma was investigated as a function of the driving frequency. The discharge was maintained, even at a pressure as low as 0.05 Torr. For this pressure, electropositive gases cannot sustain a steady state glow discharge.

In this paper we present results from ongoing work on rf discharges in SF_6. The results are from numerical simulations based on the relaxation continuum (RCT) model [14]. The primary interest of this study is the structure and function of the narrow-gap reactive-ion etcher (RIE) at 13.56 MHz. The low frequency discharge profile (100 kHz and 800 kHz) results from numerical modeling will be discussed elsewhere.

In Sec. II the RCT model will be described and developed for a system where the majority of charged particles are the positive and negative ions in the bulk plasma. The results of the present study on rf discharges at pressures of 0.5 Torr in SF_6 will be discussed in Sec. III A. In Sec. III B a quantitative comparison between previous experiments [9,15] and the present numerical results is presented. In Sec. III C the power and pressure dependences of the discharge structure are discussed. The functional properties of the narrow-gap RIE are summarized in Sec. III D, while concluding remarks are presented in Sec. IV.

II. CHARGED PARTICLE TRANSPORT IN SF_6 AND THE GOVERNING EQUATIONS

A. Charged particle transport in SF_6

Well known electron impact attachment reactions and successive negative ion-molecule reactions indicate several kinds of negative ions should be present in SF_6 discharges. The most abundant positive ion is known to be SF_5^+ from mass spectrometric measurements on dc discharges in SF_6 [16,17].

The attachment cross section Q_a for SF_6^- formation has an extremely large maximum, 5.2×10^{-14} cm^2, at the minimum energy limit of 0.0 eV [18]. The SF_n^- ($n=2,5$), F_2^-, and F^- are formed by the direct dissociative attachment from SF_6. The Q_a for SF_5^- and F^- formation have local peaks of 8×10^{-16} cm^2 (at 0.38 eV) and 6×10^{-18} cm^2 (at 5.2 eV) [19,20], respectively. The SF_5^+ is produced by electron impact ionization of SF_6, and the cross section Q_i is taken from Ref. [21]. The set of electron impact cross sections for SF_6 [22] presently used is shown in Fig. 1. Also shown are the cross sections for electronic excitations to $N_2(C\,^3\Pi_u)$ and $N_2^+(B\,^2\Sigma_u^+)$ from the ground state $N_2(X\,^1\Sigma_g^+)$ [23], since both excited species were employed as monitors of the spatiotemporal structure of SF_6 discharges in R1 and R2. Therefore, our model includes the three negative ions, SF_6^-, SF_5^-, and F^-, in addition to the positive ion SF_5^+ and the electron. The transport parameters for these ions can be found in the literature. The drift velocities v_d and the longitudinal diffusion coefficients D_L for SF_5^-, SF_6^-, and SF_5^+ were taken from Refs. [24,25]. The values of v_d and D_L of the F^- ion were taken from Ref. [26]. The ion-molecule reactions of SF_6 included in the present study are listed in Table I. The rate coefficients for the ion-molecule reactions in Table I are from Refs. [27–30], except for the recombination coefficient. The rate coefficients are a function of the reduced field strength E/N (E: field; N: neutral number density). The recombination coefficient between the positive and negative ions is estimated at 3.6×10^{-8} cm^3 s^{-1} at 0.5 Torr, from an extrapolation of the value at high pressure [31].

The electrons detached from the negative ions mentioned above might be the dominant electrons which sustain the periodic steady state rf discharge, although no evidence for this was detected in previous observations described in R1.

Experiments in a drift tube demonstrate that the

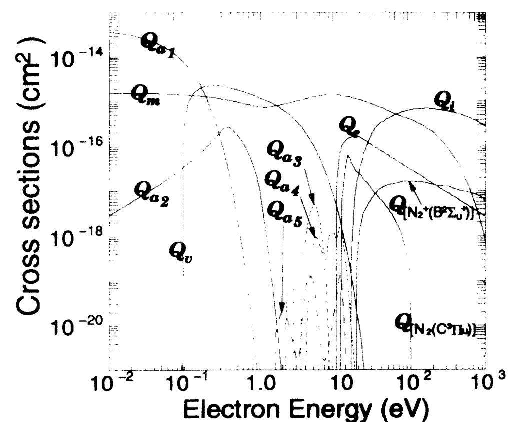

FIG. 1. Collision cross sections for electrons in SF_6 used in this work. Here Q_m is the momentum transfer cross section. The cross section for each type of electron attachment is denoted by Q_{a_j} ($j=1-5$) [22]. Q_v and Q_e are the vibrational and electronic excitation cross sections, respectively, and Q_i is the ionization cross section. $Q_{[N_2(C\,^3\Pi_u)]}$ and $Q_{[N_2^+(B\,^2\Sigma_u^+)]}$ represent the excitation cross sections of $N_2(C\,^3\Pi_u)$ and $N_2^+(B\,^2\Sigma_u^+)$ from the ground state of $N_2(X\,^1\Sigma_g^+)$, respectively.

TABLE I. Production and destruction processes of each charged particle in the SF_6 discharge considered in this work. The collisional rates due to electron impact are calculated using the Boltzmann equation and correspond to those shown in Fig. 2.

	Electron collisions		
SF_6+e	$\longrightarrow SF_5{}^+ + F + e + e$	k_i	Dissociative ionization
SF_6+e	$\longrightarrow SF_6^-$	k_{a_1}	Nondissociative attachment
SF_6+e	$\longrightarrow SF_5{}^- + F$	k_{a_2}	Dissociative attachment
SF_6+e	$\longrightarrow F^- + SF_5$	k_{a_3}	Dissociative attachment
	Ion-molecule collisions		
$SF_6+SF_6^-$	$\longrightarrow SF_5{}^- + F + SF_6$	k_1	Dissociative ion conversion
$SF_6+SF_6^-$	$\longrightarrow F^- + SF_5 + SF_6$	k_2	Dissociative ion conversion
$SF_6+SF_5^-$	$\longrightarrow F^- + SF_4 + SF_6$	k_3	Dissociative ion conversion
SF_6+F^-	$\longrightarrow SF_6{}^- + F$	k_4	Charge transfer
SF_6+F^-	$\longrightarrow SF_6 + F + e$	k_5	Electron detachment
$SF_6+SF_6^-$	$\longrightarrow SF_6{}^{-*} + SF_6$	k_6	Excitation
$SF_6+SF_6^{-*}$	$\longrightarrow SF_6 + SF_6{}^-$	k_7	Deexcitation
SF_6^-	$\longrightarrow SF_6 + e$	k_8	Autodetachment

fast detachments from $SF_5{}^-$ and $SF_6{}^-$ are insignificant [30,32]. The effective detachment coefficient is given by [27,29]

$$k_{\text{eff}} = k_5\left(\frac{k_1+k_2}{k_4+k_5}\right) + k_8\left(\frac{k_6}{k_8+k_7N}\right). \quad (1)$$

The reaction processes and related rate coefficients in Eq. (1) are listed in Table I. Equation (1) consists of two terms, the first is independent of pressure and denotes the various ion conversions and the direct detachment from F^-. The second expresses the pressure dependence of the direct detachment from $SF_6{}^-$. Under the present discharge conditions (0.05–1.0 Torr), the lifetime for autodetachment τ ($= k_8{}^{-1}$) ranges from 50 μs to 10 ms [33]. The inequality $k_7N \gg k_8$ is then satisfied and the effective detachment coefficient is, for practical purposes, given by the first term in Eq. (1). Therefore, the reactions having the rates k_6, k_7, and k_8 are not considered

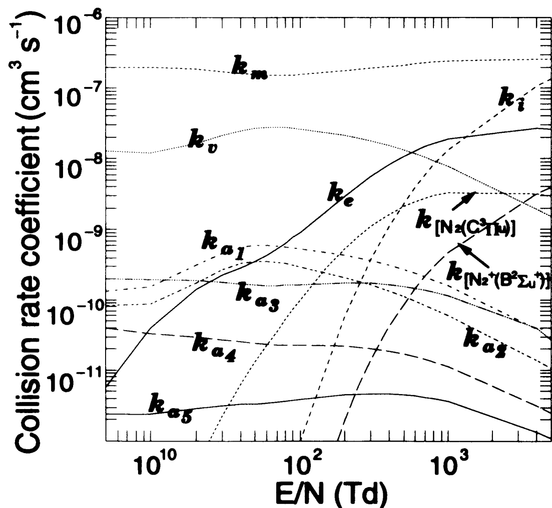

FIG. 2. The collisional rate coefficients for electrons in SF_6 as a function of the static reduced field strength E/N. Each coefficient is derived from rate corresponds to the collision cross sections shown in Fig. 1.

in this work. The threshold energy for the collisional detachment of an electron from F^- is 8 eV, while the threshold values from $SF_6{}^-$ and $SF_5{}^-$ are 90 eV. Therefore, only the collisional electron detachment from F^- is included in these simulations.

The three-dimensional velocity distributions of electrons in SF_6 are numerically calculated using the finite element method to solve the Boltzmann equation [34,35]. The collisional rate coefficients along with the transport parameters of the electrons in SF_6 are derived, over a wide range of static E/N from a value of a few Td (1 Td $= 10^{-17}$ V cm^2) to several thousand Td (see Fig. 2).

B. Governing equations

The practical narrow-gap RIE consists of parallel plate electrodes and can be modeled in one dimension by considering infinite parallel plates separated by an electrode distance of 20 mm. The schematic diagram illustrating the plasma reactor and the charged particles under consideration is shown in Fig. 3.

The system of governing equations is similar to that described in Ref. [14], except for the inclusion of momentum relaxation of the ions. It has been found that in electropositive gases the delay in momentum transfer of the ions has only a slight influence on the entire profile of the rf glow discharge, since most of the current in the bulk plasma is carried by the electrons. The situation, however, is quite different in the case of electronegative gases, since the ion densities are much higher than that of the electrons, and a considerable fraction of the current in the bulk plasma is carried by several kinds of ions. Therefore, the momentum relaxation equations for the elementary ions $SF_5{}^+$, $SF_6{}^-$, $SF_5{}^-$, and F^- must be included. The RCT model for a system where the positive and negative ions are the predominant carriers in the bulk plasma is developed as follows.

The continuity equation is

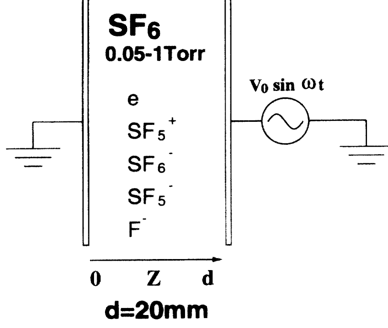

FIG. 3. Schematic diagram illustrating the geometry of the plasma reactor and the charged particles considered in this study.

$$\frac{\partial n_e}{\partial t} = \left(k_i - \sum_{k=1}^{3} k_{a_k}\right) N n_e + k_5 N n_{n_3} - \frac{\partial}{\partial z}\left(n_e v_{de} - D_{L_e}\frac{\partial n_e}{\partial z}\right), \quad (2)$$

$$\frac{\partial n_p}{\partial t} = k_i N n_e - \sum_{k=1}^{3} k_{r_i} n_p n_{n_k} - \frac{\partial}{\partial z}\left(n_p v_{dp} - D_{L_p}\frac{\partial n_p}{\partial z}\right), \quad (3)$$

$$\frac{\partial n_{n_k}}{\partial t} = k_{a_k} N n_e - k_{r_i} n_p n_{n_k} - \frac{\partial}{\partial z}\left(n_{n_k} v_{dn_k} - D_{L_{n_k}}\frac{\partial n_{n_k}}{\partial z}\right) - \sum_k k_k N n_{n_k} + \sum_k k_l N n_{n_l}; \quad (4)$$

the momentum relaxation equation is

$$\frac{\partial(m_k \boldsymbol{v_{dk}})}{\partial t} = e\boldsymbol{E} - k_{m_k} N m_k \boldsymbol{v_{dk}} - m_k \boldsymbol{v_{dk}}\frac{\partial \boldsymbol{v_{dk}}}{\partial z}; \quad (5)$$

the effective field equation is

$$\frac{\partial(n_e E_{\rm eff}^2)}{\partial t} = -\frac{E_{\rm eff}^2 - E^2}{\tau_{\varepsilon_i}} n_e - \frac{\partial}{\partial z}\left(n_e v_{de} E_{\rm eff}^2 - D_{L_e}\frac{\partial(n_e E_{\rm eff}^2)}{\partial z}\right); \quad (6)$$

and Poisson's equation is

$$\frac{\partial E}{\partial z} = -\frac{\partial^2 V}{\partial z^2} = \frac{e}{\epsilon_0}\left(n_p - n_e - \sum_{k=1}^{3} n_{n_k}\right), \quad (7)$$

where $n_e, n_p, n_{n_1}, n_{n_2}, n_{n_3}$, and N are the number densities of the electron, SF_5^+, SF_6^-, SF_5^-, F^-, and SF_6, respectively. The mass and charge of the electron and each ion are, respectively, denoted by m_k and e. The letters V and E are the potential and the electric field, while k_i, k_a, and k_r are the respective ionization, electron attachment, and recombination rate coefficients. The coefficient k_{m_k} represents the momentum-transfer rate coefficient for each of the charged particles. The relaxation time τ_{ε_i} in Eq. (6) is defined in this study as

$$\tau_{\varepsilon_i}{}^{-1} = \frac{\sum_j \int_{v_i}^{\infty} N Q_j(v) v g(\boldsymbol{v}) dv}{\int_{v_i}^{\infty} g(\boldsymbol{v}) dv}, \quad (8)$$

where $Q_j(v)$ is the inelastic cross section above the ionization threshold energy $m_e v_i{}^2/2$ and $g(\boldsymbol{v})$ is the velocity distribution of the electrons as a function of static E/N. The ionization rate coefficient k_i is then determined by the function $E_{\rm eff}(z,t)/N$ from values previously obtained under uniform and constant (static) reduced field strengths. Each of the rate coefficients used in Eqs. (2)–(6) corresponds to a reaction processes listed in Table I.

III. RESULTS AND DISCUSSION

A. Discharge structure in the narrow-gap RIE

The numerical calculations were performed for pressures between 0.05 Torr and 1.0 Torr, under external discharge conditions similar to those in the previous experiments discussed in R1 and R2. The applied voltage between the electrodes has the wave form

$$V_{\rm app}(t) = V_0 \sin\omega t, \quad (9)$$

where V_0 is the input voltage, ω the frequency, and t the time. The configuration of the rf discharge at 0.5 Torr is the main one presented and discussed in this work, since the structure at this pressure represents the typical properties of the narrow-gap RIE.

Figure 4 shows the spatial density distributions of the

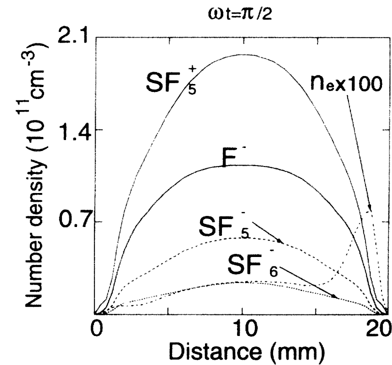

FIG. 4. Spatial density distributions of the positive and negative particles in the SF_6 discharge at the phase $\omega t = \pi/2$ under conditions of f = 13.56 MHz, V_0 = 200 V, W = 140 mW cm^{-2}, and p = 0.5 Torr. The electron density n_e has been magnified by a factor of 100.

positive and negative species in the periodic steady state SF_6 discharge at a phase of $\omega t = \pi/2$ under conditions of $f = 13.56$ MHz, $V_0 = 200$ V, $p = 0.5$ Torr, and $W = 140$ mW cm^{-2}. Several peculiar characteristics are found as compared with those observed in electropositive gases. First, the plasma density is greater than that found in electropositive gases by two orders of magnitude. Second, the majority of charged particles consists of the positive and negative ions, while electrons are in the minority. The electron density is three orders of magnitude less than the positive ion density in the center of the bulk plasma. Third, the electron density exhibits two maxima during one period in front of the instantaneous anode. The large difference between the magnitudes of the electron and positive ion densities at the center of the bulk plasma represents a unique characteristic of the discharge structure. The difference affects external electrical characteristics of the narrow-gap RIE studied experimentally in R1 and R2. The local peak in the electron density in front of the instantaneous anode shown in Fig. 4 can be understood from the spatiotemporal density distribution of electrons displayed in Fig. 5. The peak exhibits a finite phase delay with respect to the applied voltage maximum by 0.2π, and the electron density at the edge of the bulk plasma propagates to the anodic side in opposition to the positive-ion sheath field. The winglike spatial distribution is realized for the electrons between the electrodes. The calculated bulk plasma density of 10^8 cm^{-3} matches Langmuir probe measurements [5].

The potential is a key parameter. Figure 6(a) shows the potential between the electrodes during one period. The plasma potential during the second half of the period is mostly negative with respect to the grounded electrode. This is quite different from a conventional plasma consisting of electrons and positive ions, which has a positive plasma potential over the entire period [36,37]. The positive plasma potential throughout the rf period results from ambipolar fields due to the difference in transport parameters of electrons and positive ions. In the strongly electronegative SF_6 plasma studied here, the majority of the charged particles are positive and negative ions having nearly the same mass as shown in Fig. 4. As a result, the plasma potential oscillates between the positive and negative values every half-period. This phenomenon is similar to that in low frequency discharges in electronegative gases [10,38], although the spatial modulation of positive and negative ions densities during the period is also important at low frequencies.

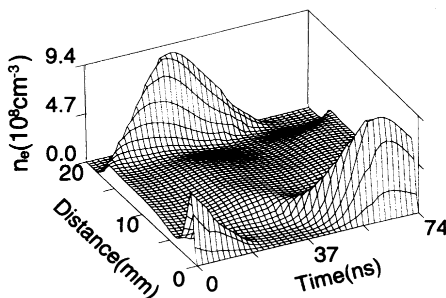

FIG. 5. Spatiotemporal density distribution of electrons n_e for a periodic steady state SF_6 discharge. The conditions are the same as those in Fig. 4.

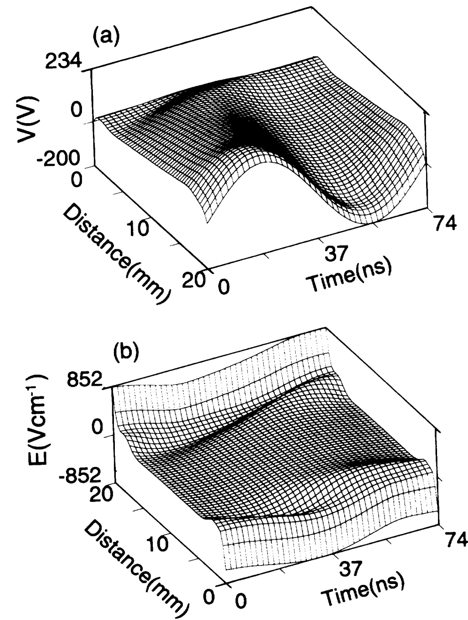

FIG. 6. The distribution of the (a) potential V and (b) electric field E in the rf glow discharge in SF_6 as functions of space and time. The conditions are the same as in Fig. 4.

Although the potential exhibits interesting characteristics in comparison to the potential of a discharge in electropositive gases, the electric field distribution in Fig. 6(b) yields more direct and important information. The collisional rate coefficient and the electron and ion transport coefficient are defined as a function of the reduced field. The field distribution has local structure, in addition to the temporal dependence in the bulk plasma and the sheath. In particular, local minimum and maximum exist in front of the rf and grounded electrodes during each anodic cycle. This is similar to that found in rf discharges in weakly electronegative SiH_4 at 13.56 MHz [39]. The local structure results from the formation of a double layer in front of the instantaneous anode. The double layer formation originates from the transient accumulation of excess negative charge in front of the electrode by the temporal modulation of electrons in the bulk plasma during the anodic part of the cycle at 13.56 MHz (see Fig. 7). The double layer can also be formed at low frequencies due to the modulation of negative ions densities [10,40]. Once the double layer is formed, electron multiplication toward the anode occurs between the layer and the electrode due to the migration of bulk electrons. As a result, the double layer and the local field peak are developed toward the anode. In particular, two types of double layers can be found in Fig. 7(a) at $\omega t = 3\pi/2$. The active double layer is formed in front of the instantaneous anode, while the passive layer remains near the cathode.

The relatively high sinusoidal field, having an amplitude of 90 V cm^{-1}, is formed in the bulk plasma to carry the massive positive and negative ions as well as electrons

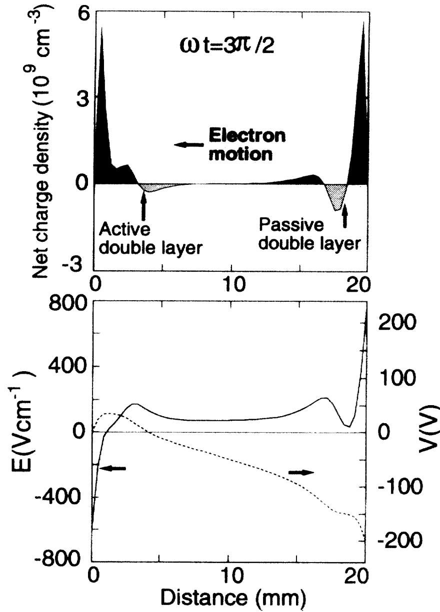

FIG. 7. Net charge density, electric field E, and potential V distributions at the phase $\omega t = 3\pi/2$. The conditions are the same as those in Fig. 4.

and maintain total current continuity at each position. The apparent sheath width is narrower in electronegative gases than in electropositive gases. This will be discussed later.

Each component of the current density J_i at $\omega t = \pi/2$ is shown in Fig. 8 as a function of position. The current behaves in a very complex manner, but can be simply explained. The total current is independent of position, due to the requirement of current continuity, and can act as an indicator of the accuracy of the numerical calculations. It is known that the drift of electrons is the main component of the current in the bulk plasma with electropositive gases [14]. The displacement component J_D as well as the drift of charged particles contribute to the total current at the center of the bulk plasma with electronegative gases as shown in Fig. 8. This is due to the higher field (90 V cm^{-1}) at the center of the bulk plasma. All components except J_D have positive values at $\pi/2$ and the electron current has a magnitude similar to that of the F^- ion current in the bulk plasma. This is reasonable because the drift velocity of the electrons is larger than that of F^- ion by three orders of magnitude, which compensates for the density difference between them shown in Fig. 4. Although the densities of massive ions $SF_5{}^+$, $SF_6{}^-$, and $SF_5{}^-$ have the same order of magnitude as that of F^-, these ion currents at $\omega t = \pi/2$ are less than J_{F^-} by a factor of 2. This can be explained by the fact that the massive ions cannot follow the instantaneous local field due to their lower mobilities. The peak value and corresponding phase of each current component at the center of the bulk plasma during the first half period are listed in Table II. The positive ion current incident on the electrode is almost constant because the time variation of the sheath field is weak. The constant ion current contrasts with that found in electropositive gases.

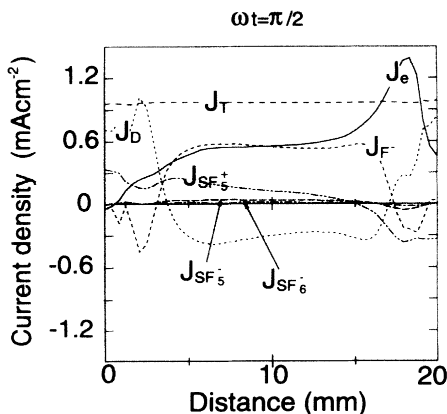

FIG. 8. The solid and dashed lines in the lower panel represent the spatial distributions of the electric field and the potential, respectively. The distribution of current for each component at a phase $\omega t = \pi/2$ as a function of position. The symbols J_T, J_e, J_p, $J_{SF_6^-}$, $J_{SF_5^-}$, J_{F^-}, and J_D represent, respectively, the total, electron, positive ion, $SF_6{}^-$, $SF_5{}^-$, F^-, and displacement current densities. The conditions are the same as those in Fig. 4.

The time variation of the total current I during one period is shown in Fig. 9 along with the wave forms of the applied voltage V and dissipated power [see Fig. 3(a) in R1]. The resistive or even slightly inductive characteristics of the rf discharge in SF_6 can be understood by considering two different mechanisms. The electron density peak in the vicinity of the instantaneous anode develops in phase with the applied voltage due to the ionization between the double layer and the anode as mentioned above. This means that the dominating electron current is in phase or has a small delay with respect to the applied voltage wave form, causing resistive or even slightly inductive characteristics. The other mechanism is from the ion transport in the bulk plasma. The ion transport (ion drift in the bulk plasma) has a finite phase delay due to the momentum-relaxation time of the massive ions. Ions carry a current comparable to that of the electrons. As a result, the total current changes from capacitive to resistive or inductive in character as the density ratio n_p/n_e increases in the bulk plasma. This results in an efficient absorption of power in an electronegative plasma reactor compared with an electropositive plasma.

TABLE II. Peak current and the phase of each charged particle flow at the center of the bulk plasma during the first half-period in the SF_6 discharge with of f = 13.56 MHz, V_0 = 200 V, W = 140 mW cm^{-2}, and p = 0.5 Torr.

Species	Peak value (mA cm^{-2})	Phase $\omega t(\pi)$
$SF_5{}^+$	0.26	0.775
$SF_6{}^-$	0.027	0.775
$SF_5{}^-$	0.076	0.775
F^-	0.98	0.725
e	0.78	0.4

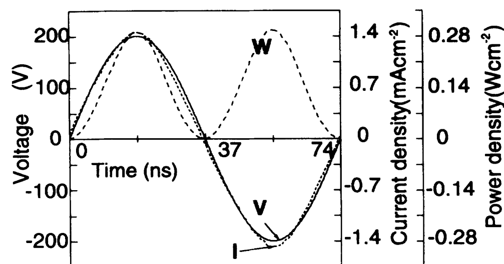

FIG. 9. The current I (dotted line), applied voltage V (solid line), and dissipated power W (dashed line) in the SF_6 discharge as a function of time. The conditions are the same as those in Fig. 4.

Figure 10 shows the net ionization rate between the electrodes during one period. The influence of the anomalous field distribution can be estimated from Fig. 10, and a possible electron source can be identified as electron detachment from negative ions. The net rate of ionization at position I is from reflected electrons at the positive ion sheath. Typically, ionization position I represents the dominant process sustaining rf discharge at 13.56 MHz in electropositive gases [10–14], although the temporal phase of the ionization is considerably different from that found here. The ionization at position II in the figure is from the electron transport in the relatively high sinusoidal field of the bulk plasma. The increased ionization at the double layer is denoted by III. The maintenance of the rf discharge in SF_6 is due to the ionization between the double layer and the instantaneous anode at III. The development of electron impact ionization toward the instantaneous anode is caused by the formation of the double layer and the consecutive electron acceleration and multiplication. With increasing input power, the ratio of the net ionization at III to other points is increased. It should be noted that the distance from the peak at III to the instantaneous anode is much shorter than that from I to the instantaneous cathode. The dominant electron detachment process is the ion-molecule reaction between F^- and SF_6, as mentioned in Sec. II [28,29]. The calculated electron detachment formation rate from F^- ion has a maximum of 3.3×10^{15} $cm^{-3}\,s^{-1}$

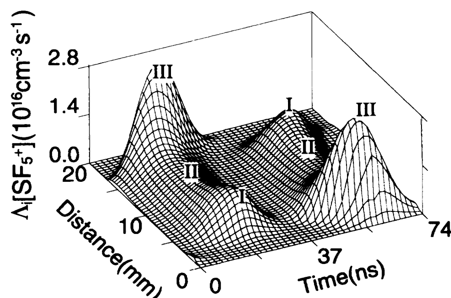

FIG. 10. Spatiotemporal distribution of the net ionization rate $\Lambda_i(z,t)$ in an rf glow discharge in SF_6 . The conditions are the same as those in Fig. 4. See the text for an explanation of the Roman numerals.

TABLE III. Production and extinction rates of the charged particles in the SF_6 discharge. The conditions are the same as those in Table II.

	Electron	
Production	ionization	96%
	detachment	4%
Extinction	flux to chamber	57%
	attachment to SF_6^-	22%
	attachment to SF_5^-	10%
	attachment to F^-	11%
	Positive ion SF_5^+	
Production	ionization	100%
Extinction	flux to chamber	78%
	recombination	22%
	Negative ion F^-	
Production	attachment	34%
	ion-molecule reactions	66%
Extinction	flux to chamber	30%
	detachment	19%
	recombination	51%

at the sheath, because the detachment rate rapidly increases with increasing field strength [27]. The peak value is one order of magnitude less than the electron impact ionization rate during the same phase as shown in Fig. 10. As a result, it is concluded that no appreciable contribution results from the detached electrons to the overall sustaining mechanism of the rf discharge in SF_6.

In summary, the production and extinction rates of the charged particles in the plasma reactor, considered in this work, are classified as to the type of process and are compared in Table III. It should be noted that more than three-fourths of the positive ions produced in the reactor are transported to the electrode surfaces and contribute to the surface reaction. The strongly electronegative character of the SF_6 discharge is indicated from the result that 43% of the electrons formed in the chamber are transferred into negative ions.

B. Comparison with experiments

The present numerical results can be quantitatively compared with experimental results. One of the most suitable comparisons involves space- and time-resolved optical emission spectroscopy (STR-OES) [9,15,41].

In the previous paper R1, the STR-OES was applied to $N_2(C\,^3\Pi_u)$ and $N_2^+(B\,^2\Sigma_u^+)$ in a mixture of gases consisting of N_2(10%) and SF_6(90%) at the central axial part of the discharge [42], in order to obtain quantitative results apart from the lack of data on electron impact excitation cross sections for SF_6. The excitation cross sections for $N_2(C\,^3\Pi_u)$ and $N_2^+(B\,^2\Sigma_u^+)$ are well known [23]. Both probe species were produced by direct electron impact excitation (ionization)

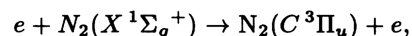

$$e + N_2(X\,^1\Sigma_g^+) \to N_2(C\,^3\Pi_u) + e, \qquad \epsilon_j = 11.03 \text{ eV}, \quad (10)$$

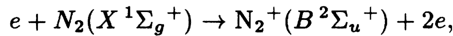

$$e + N_2(X\,^1\Sigma_g{}^+) \rightarrow N_2{}^+(B\,^2\Sigma_u{}^+) + 2e,$$

$$\epsilon_i = 18.75 \text{ eV}. \quad (11)$$

The cross section for $N_2(C\,^3\Pi_u)$ has a sharp peak near the threshold and is small above 20 eV, while the cross section for $N_2{}^+(B\,^2\Sigma_u{}^+)$ exhibits a broad maximum near 100 eV. Thus the net excitation rate of $N_2(C\,^3\Pi_u)$ will yield information on electron kinetics around 15 eV, while the net ionization rate of $N_2{}^+(B\,^2\Sigma_u{}^+)$ can be used as a monitor of the electrons well above the 20 eV. These two rates provide information on the behavior of middle-energy and high-energy electrons. In order to obtain numerical results for comparison with the previous experiments, the numerical calculations of the net production rates in Eqs. (10) and (11) have been performed using the rate coefficients for SF_6(90%)-N_2 and the assumption that the addition of 10% N_2 results in no significant change in the spatiotemporal discharge structure. This has been confirmed experimentally (see papers R1 and R2).

Although the numerically calculated excitation rate $\Lambda_j(z,t)$ is large compared with the experimental rates for $N_2{}^+(B\,^2\Sigma_u{}^+)$ and $N_2(C\,^3\Pi_u)$ in Figs. 11 and 12, respectively, the phase, peak position, and absolute magnitude of both results are in reasonable agreement. The temporal ridges in the production rate of $N_2{}^+(B\,^2\Sigma_u{}^+)$ at $\omega t = \pi/2$ and $3\pi/2$ during a period have the same values. The calculated peak magnitude at 2.0 mm in front of the instantaneous anode is nearly the same as the experimental peak at 1.0 mm. Overall, the calculated net production rate for $N_2{}^+(B\,^2\Sigma_u{}^+)$ exhibits good agreement

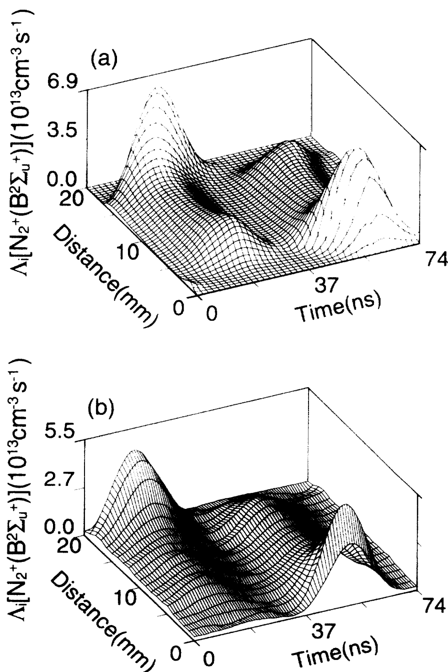

FIG. 11. Comparison of the space-time-resolved net production rate $\Lambda_i(z,t)$ of $N_2{}^+(B\,^2\Sigma_u{}^+)$ determined (a) theoretically and (b) experimentally in a $SF_6(90\%)/N_2$ discharge with $f = 13.56$ MHz, $p = 0.5$ Torr, and $W = 140$ mW cm^{-2}.

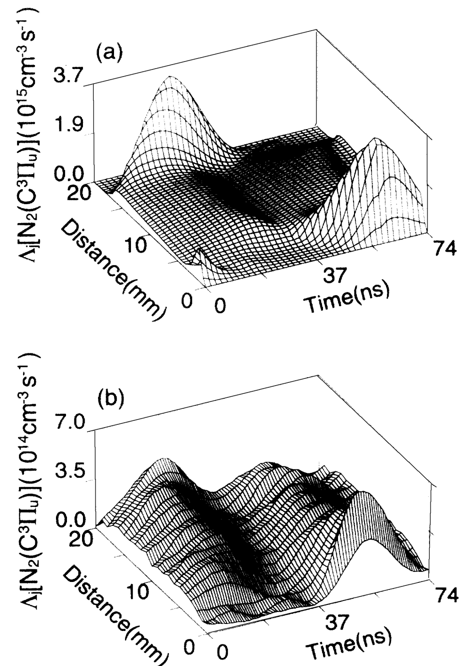

FIG. 12. Comparison of the space-time-resolved net production rate $\Lambda_j(z,t)$ of $N_2(C\,^3\Pi_u)$ determined (a) theoretically and (b) experimentally in a SF_6(90%)-N_2 discharge. The conditions are the same as those in Fig. 11.

with experimental results. These results are demonstrative proof that the higher energy electrons with $\epsilon \geq 18.75$ eV are well described in the present modeling.

The other comparison involving the net excitation rate of $N_2(C\,^3\Pi_u)$ is shown in Fig. 12. The values of the simulation are 5 times larger than the experimental values at the peak in the sheath. At the center of the bulk plasma, both results agree rather well with a peak value of 3.4×10^{14} cm^{-3} s^{-1} at $\omega t = 0.55\pi$. This is mainly due to the overestimation of the production rate between the double layer and the instantaneous anode. This can be inferred from the fact that ion transport to the electrode is overestimated in this numerical model.

C. Power and pressure dependences on the discharge structure

The time-averaged net ionization rate $\Lambda_i(z)$ as a function of distance for various amplitudes of the applied voltage is shown in Fig. 13. As the applied voltage is increased, a broad peak gradually separates from the sharp peak near the electrode. At $V_0 = 350$ V, two distinct peaks can be seen in front of each electrode. The sharp and broad peaks, respectively, result from the ionization by electrons moving toward the electrode from the double layer and from the ionization by reflected electrons in front of the electrode. These sharp and broad peaks correspond to III and I in Fig. 10. It should be noted that the sheath width decreases as the applied voltage (input power) increases due to the development of the double

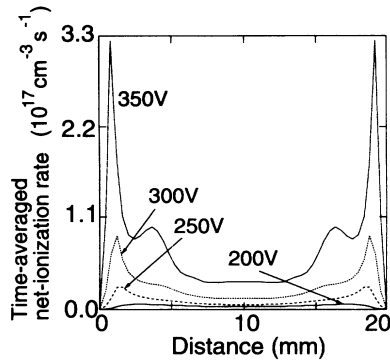

FIG. 13. Spatial dependence of the time-averaged net ionization rate $\Lambda_i(z)$ in a SF_6 discharge for various values of the applied voltage V_0 with f=13.56 MHz and p=0.5 Torr.

layer. The excited or dissociated molecules are also produced by electron impact with a profile similar to that for the ionization, as shown in Figs. 10 and 13. This means that the virgin radical as well as the ions, formed immediately in front of the electrode, can be transported to the electrode with little reaction with background molecules.

In previous experimental work discussed in R1 and R2, it was shown that a parallel plate rf discharge in SF_6 with a distance of 20 mm between the electrodes can be sustained down to a pressure of 0.05 Torr. It is important to investigate whether or not the discharge structure changes at pressure of 0.05 Torr, since some dry etchers operate at the lowest pressure that can be sustained. Figures 14(a) and 14(b) show, respectively, the theoretical and experimental spatiotemporal profiles of the net ionization rate of $N_2{}^+(B\,^2\Sigma_u{}^+)$. The theoretical external discharge conditions $p = 0.05$ Torr and $W = 21$ mW cm^{-2} are the same as the experimental values. The maxima in the net production rate appear at approximately the same position in front of the instantaneous anode. The maxima in Figs. 14(a) and 14(b) during the first half-period occur at ($\omega t = 0.35\pi, z = 17.6$ mm) and ($\omega t = 0.39\pi, z = 18$ mm), respectively. The density distribution at $\omega t = \pi/2$ for each charged particle is shown in Fig. 15. The spatial profiles of the positive and negative ions are independent of time, while the electron density is temporally modulated by a profile similar to the net ionization rate of $N_2{}^+(B\,^2\Sigma_u{}^+)$ in Fig. 14(a). Here it should be recalled that an electronegative discharge widens bulk plasma region compared to an electropositive discharge, due to the great difference in the transport coefficient of the electrons and negative ions. In the present case, as shown in Fig. 14, the electron avalanche develops under a relatively high accelerating field (45 V cm^{-1}) in the bulk plasma. As a result, two peaks in the net rate appear in front of the instantaneous anode. Even at pressures of 0.05 Torr, a small double layer can be discerned in the vicinity of the anode having a negative net charge density peaking at -3×10^7 cm^{-3} at $\omega t = 0.9\pi$ and $z = 15.2$ mm. It is found that the discharge is maintained by the ionization near the instantaneous anode. Overall, the positive ion sheath becomes narrower due to the ionization in front of the instantaneous anode and due to a wider bulk plasma, as compared to systems with electropositive gases. The rate of electron production by the collisional detachment from the F^- ion is only 1% of the rate of electron impact ionization, and therefore the electrons resulting from detachment have no significant influence on the discharge structure.

Figure 16 shows the phase difference φ between the total current and the sustaining voltage as a function of power deposition in the narrow-gap RIE for various values of total pressure. The positive and negative values of φ correspond to a capacitive or inductive rf discharge, respectively. The numerically calculated and experimental characteristics at 0.5 and 1.0 Torr rapidly change

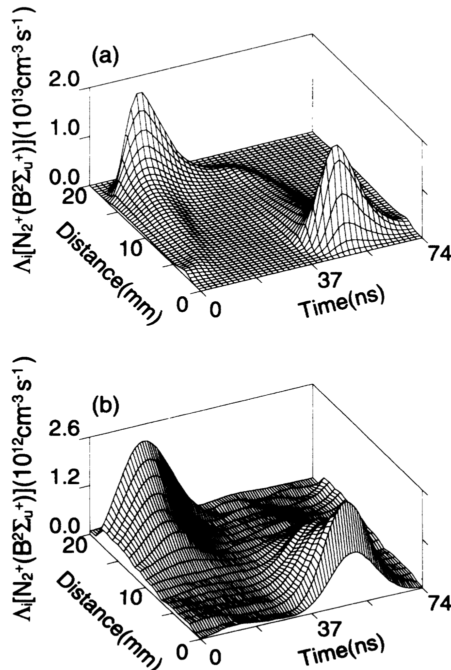

FIG. 14. Comparison of the space-time-resolved net production rate $\Lambda_i(z,t)$ of $N_2{}^+(B\,^2\Sigma_u{}^+)$ determined (a) theoretically and (b) experimentally in a SF_6(90%)/N_2 discharge with $f = 13.56$ MHz, $p = 0.05$ Torr, and $W = 21$ mW cm^{-2}.

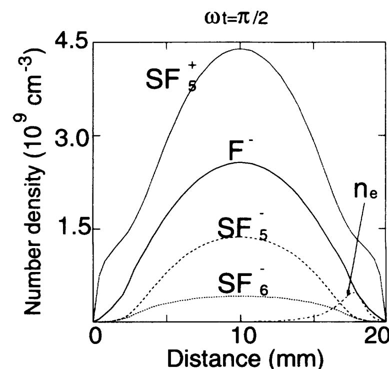

FIG. 15. Spatially resolved density of each charged particle at a phase of $\omega t = \pi/2$. The conditions are the same as those in Fig. 14.

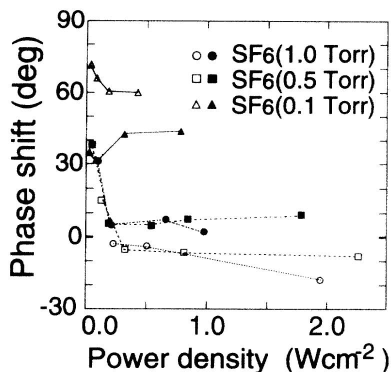

FIG. 16. Phase shift between the total current $I(t)$ and the sustaining voltage $V(t)$ as a function of dissipated power density for various pressures denoted in the upper right-hand corner. The symbols ●, ▲, ■ are experimental values, while ○, △, □ are theoretical values.

from capacitive to resistive at 0.25 W cm^{-2}, although a weakly inductive behavior is indicated in the theoretical results. This means that the numerically calculated negative ion density is slightly overestimated. The discharge at 0.1 Torr is essentially capacitive and independent of the power density.

It can be concluded that the present numerical results using the RCT model can reproduce both the spatiotemporal structure and the external electrical characteristics of the rf discharge in SF_6 at 13.56 MHz.

D. Function of narrow-gap RIE

The source gases must first be classified as electropositive or negative gases when discussing the function of the narrow-gap RIE. In a rf discharge with an electronegative gas, in which the positive and negative ions act as the majority of charged particles, an asymmetric configuration of the electrodes in the RIE is less effective in producing the asymmetric discharge with a stronger positive-ion sheath in front of the smaller electrode. The dc self-bias voltage which occurs in electropositive discharges is not expected to occur in electronegative discharges. This leads to a somewhat different conclusion about the dominant mechanism of the RIE. High energy positive ions are produced in electropositive discharges in the strong sheath field from the dc self-bias voltage due to the asymmetry of the electrodes [43]. The proposed mechanism that furnishes the beamlike ions to the surface with a high degree of efficiency is from the narrower positive ion sheath due to the wide diffusion controlled bulk plasma. The wide bulk plasma can be attributed to the constituents of the bulk plasma. The positive and negative ions are the majority of charged particles, as discussed in Sec. III A. The main function of the narrow-gap RIE under typical operating conditions is controlled by the double layer in front of the electrode. The double layer acts as the source of virgin radicals immediately in front of the electrode surface.

IV. CONCLUDING REMARKS

Various kinds of reactive electronegative gases have been employed in dry etching processes for microelectronic device fabrication, selected for their etching ability and for the type of volatile compounds formed in chemical reactions with the masked-solid surface. As discussed in Sec. III, the advantage of electronegative gases used in plasma etching with a narrow-gap RIE can be understood from the viewpoint of discharge physics with stable negative ions.

The diffusion controlled bulk plasma is formed by the majority positive and negative ions in the narrow-gap RIE over a range of pressure from the lowest pressure to several Torr. The resulting double layer acts as the source of beamlike ions and virgin radicals immediately in front of the electrode surface. Another advantage is the realization of a relatively low pressure plasma. This is possible because the system consists of positive and negative ions as the majority of charged particles, with a minority of electrons. The numerical simulations based on the RCT model of the narrow-gap RIE in SF_6 are in good agreement with experimental results on the net production rate of excited molecules and ions.

Several mechanisms proposed in two previous papers (R1 and R2) for the formation of the spatial as well as temporal structure of SF_6 at 13.56 MHz were confirmed in this paper. This was accomplished by achieving reasonably good quantitative agreement between the theoretical and experimental net excitation rates. The especially good agreement on the net ionization rate of $N_2^+(B\,^2\Sigma_u^+)$ is important for calculation of the electrical characteristics of the discharge as well as the simulation of the major sustaining mechanisms.

ACKNOWLEDGMENTS

This work was supported in part by a Grant-in-Aid for Scientific Research No. B-05452106 and on Priority Areas, "Control of Reactive Plasmas" and "Free Radical Science," from the Ministry of Education, Science and Culture in Japan.

[1] *Dry Etch Technology in Microelectronic Device Fabrication*, edited by T. Tokuyama (Sangyo-Tosyo, Tokyo, 1992) (in Japanese).

[2] G. Turban, J.F. Coulon, and N. Mutsukura, Thin Solid Films **176**, 289 (1989).

[3] Y.J. Lii, J. Jorné, K.C. Cadien, and J.E. Schoenholtz, Jr., J. Electrochem. Soc. **137**, 3633 (1989).

[4] A.P. Paranjpe, J.P. McVittie, and S.A. Self, J. Vac. Sci. Technol. A **8**, 1654 (1990).

[5] A.P. Paranjpe, J.P. McVittie, and S.A. Self, Phys. Rev. A **41**, 6949 (1990).

[6] E. Gogolides, J.P. Nicolai, and H.H. Sawin, J. Vac. Sci. Technol. A **7**, 1001 (1989).

[7] E. Gogolides and H.H. Sawin, J. Appl. Phys. **72**, 3971

(1992).
[8] E. Gogolides and H.H. Sawin, J. Appl. Phys. **72**, 3988 (1992).
[9] Z.Lj. Petrović, F. Tochikubo, S. Kakuta, and T. Makabe, J. Appl. Phys. **73**, 2163 (1993).
[10] J.-P. Boeuf, Phys. Rev. A **36**, 2782 (1987).
[11] C.G. Goedde, A.J. Lichtenberg, and M.A. Lieberman, J. Appl. Phys. **64**, 4375 (1988).
[12] D. Vender and R.W. Boswell, IEEE Trans. Plasma Sci. **18**, 725 (1990).
[13] M. Surendra, D.B. Graves, and I.J. Morey, Appl. Phys. Lett. **56**, 1022 (1990).
[14] T. Makabe, N. Nakano, and Y. Yamaguchi, Phys. Rev. A **45**, 2520 (1992).
[15] S. Kakuta, Z.Lj. Petrović, F. Tochikubo, and T. Makabe, J. Appl. Phys **74**, 4923 (1993).
[16] I. Sauers and G. Harman, J. Phys. D **25**, 761 (1992).
[17] J.J. Wagner and W.W. Brandt, Plasma Chem. Plasma Processing **1**, 201 (1981).
[18] A. Chutjian, Phys. Rev. Lett. **46**, 1511 (1981).
[19] B. Lehmann, Z. Naturforsch. A **25**, 1755 (1970).
[20] L.E. Kline, D.K. Davies, C.L. Chen, and P.J. Chantry, J. Appl. Phys. **50**, 6789 (1979).
[21] D. Rapp and P. Englander-Golden, J. Chem. Phys. **43**, 1464 (1965).
[22] H. Itoh, Y. Miura, N. Ikuta, Y. Nakao, and H. Tagashira, J. Phys. D **21**, 922 (1988).
[23] A.V. Phelps and L.C. Pitchford, Phys. Rev. A **31**, 2932 (1985).
[24] J. de Urquijo, I. Alvarez, C. Cisneros, and H. Martínez, in *Nonequilibrium Effects in Ion and Electron Transport*, edited by J.W. Gallagher, D.F. Hudson, E.E. Kunhardt, and R.J. Van Brunt (Plenum Press, New York, 1990), pp. 211–227.
[25] J. de Urquijo, I. Alvarez, H. Martínez, and C. Cisneros, J. Phys. D **24**, 664 (1991).
[26] Y. Nakamura, J. Phys. D **21**, 67 (1988).
[27] J.K. Olthoff, R.J. Van Brunt, Y. Wang, L.D. Doverspike, and R.L. Champion, in *Nonequilibrium Effects in Ion and Electron Transport* (Ref. [24]), pp. 229–244.
[28] Y. Wang, R.L. Champion, L.D. Doverspike, J.K. Olthoff, and R.J. Van Brunt, J. Chem. Phys. **91**, 2254 (1989).
[29] J.K. Olthoff, R.J. Van Brunt, Y. Wang, R.L. Champion, and L.D. Doverspike, J. Chem. Phys. **91**, 2261 (1989).
[30] Y. Nakamura, in *Nonequilibrium Effects in Ion and Electron Transport* (Ref. [24]), pp. 197–210.
[31] R. Morrow, IEEE Trans. Plasma Sci. **PS-14**, 234 (1986).
[32] B.C. O'Neil and J.D. Craggs, J. Phys. B **6**, 2634 (1973).
[33] R.W. Odom, D.L. Smith, and J.H. Futrell, J. Phys. B **8**, 1349 (1975).
[34] J.P. Balaguer, P. Segur, M.C. Bordage, and M. Yousfi, J. Comp. Phys. **50**, 116 (1983).
[35] N. Shimura and T. Makabe, J. Phys. D **25**, 751 (1992).
[36] A.D. Richards, B.E. Thompson, and H.H. Sawin, Appl. Phys. Lett. **50**, 492 (1987).
[37] R.W. Boswell and I.J. Morey, Appl. Phys. Lett. **52**, 21 (1988).
[38] R.A. Gottscho and C.E. Gaebe, IEEE Trans. Plasma Sci. **PS-14**, 92 (1986).
[39] T. Makabe, F. Tochikubo, and M. Nishimura, Phys. Rev. A **42**, 3674 (1990).
[40] R.A. Gottscho, Phys. Rev. A **36**, 2233 (1987).
[41] F. Tochikubo, T. Kokubo, S. Kakuta, A. Suzuki, and T. Makabe, J. Phys. D **23**, 1184 (1990).
[42] F. Tochikubo and T. Makabe, Meas. Sci. Technol. **2**, 1133 (1991).
[43] B. Chapman, *Glow Discharge Processes—Sputtering and Plasma Etching* (John Wiley & Sons, New York, 1980).

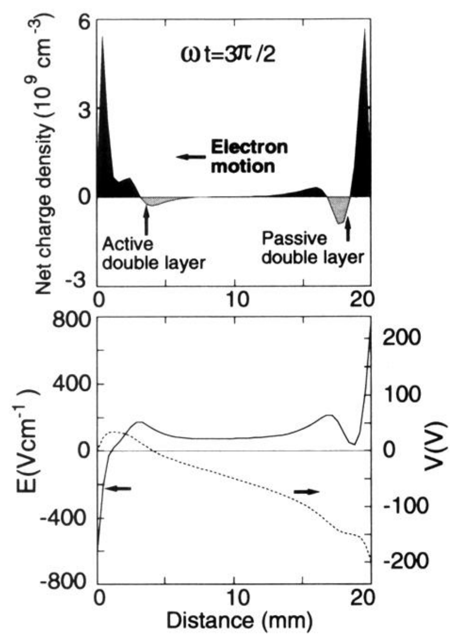

FIG. 7. Net charge density, electric field E, and potential V distributions at the phase $\omega t = 3\pi/2$. The conditions are the same as those in Fig. 4.